December 29, 2005

Radio and Hard X-Ray Imaging Observations of the M 5.7 Flare of 2002 March 14

E.J. Schmahl[1,2], M.R. Kundu[1], and V.I. Garaimov[1]

[1]*Astronomy Department, University of Maryland, College Park, MD 20742*
[2]*Lab for Astronomy and Solar Physics, NASA Goddard Space Flight Center, Greenbelt, MD 20771*

ABSTRACT

We describe a flare of GOES class M5.7 which was observed simultaneously by RHESSI (Ramaty High Energy Solar Spectroscopic Imager) and NoRH (Nobeyama Radio Heliograph). The flare occurred in active region AR 9866 located near disk center. The hard X-ray, microwave, EIT and TRACE 195 Å observations indicate that the flaring region consisted of a complex of multiple loops. In the microwave domain the source morphology, the timing, the polarization characteristics, and the photospheric magnetic fields indicate clearly that it is of a class characterized as a "double loop" configuration, meaning two systems of magnetic flux, each consisting of many smaller loops. The observations suggest the existence of a small loop system created by the emergence of new flux, which interacts with an old flux system and of a remote flare site which is observed primarily in radio. The former is the main flare site where we observe microwave, HXR, and EUV emissions. In HXR there are two main identifiable loop systems, an elongated one filled with energetic electrons primarily emitting lower energy (12-25 keV) HXR with a co-located microwave source; this source has distinct foot points at higher X-ray energies. The second loop system is implied by compact HXR sources in opposite magnetic polarities separated by a distance greater than the length of the first loop system. Spectroscopic analysis of the RHESSI data shows that the spectrum can be fitted with a thick-target model with a thermal component and a broken power-law component of the electron energy distribution. This model is used to address the thermal/nonthermal and radio/HXR electron number problems.

Subject headings: Sun: corona — Sun: flares — Sun radio radiation — Sun: x-rays

1. INTRODUCTION

It has been known for a long time that flares occur in regions consisting of many magnetic loops and that a flare can be caused by the interaction between loops. Evidence of interaction between newly emerging flux and overlying magnetic fields causing flares have been provided from optical observations (see e.g. Zirin 1983; Kurokawa 1989), and soft X-ray observations from Yohkoh have provided evidence of interactions between coronal loops (e.g. Hanaoka 1994; Inda-Koide *et al.* 1995; Shimuzu *et al.* 1994). Only a limited number of observations of interacting flaring loops exist in the radio domain, primarily due to lack of good enough spatial resolution to demonstrate the existence of such interacting loops (see e.g. Kundu *et al.* 1982; Kundu & Shevgaonkar 1985). More recently because of observations made with the solar dedicated Nobeyama Radio Heliograph (NoRH) at 17 and 34 GHz, it has been possible to analyze a large number of flares and show evidence of interacting loops, although the spatial resolution was only of order $5'' - 10''$. Thus, Hanaoka (1996, 1997, 1999) and Kundu *et al.* (2001) provided evidence that emerging flux appeared near one sunspot–dominated active region and argued that interactions between this emerging flux and the overlying loop resulted in the onset of flares and microflares. The main flare site in each case was the location of emerging flux which was also the location of soft X-ray and EUV brightening. In addition the NoRH images showed that at 17 GHz a compact brightening occurred at the main flare site as well as at a remote region whose polarity was opposite to the dominant polarity (the eastern component) of the main flare. This observation obviously means a double magnetic configuration of the flaring source, where high energy electrons generated or accelerated at the main flare site propagate over to the remote site. At this remote site, polarized microwave radio emission appeared, but hard X-rays were weak or non-existent.

In this paper we discuss a solar flare with similar magnetic field topology. Unlike previous papers dealing with a "double-loop" configuration, we have RHESSI (Ramaty High Energy Solar Spectroscopic Imager) imaging observations of hard X-rays of energy up to ~ 200 keV. Since RHESSI has more sensitivity, dynamic range, and better spatial resolution than Yohkoh/HXT, it is useful to check if the remote site of the "double-loop" system configuration does indeed produce only the radio emission or emit both radio and HXR emissions. One important objective of studying hard X-ray and microwave images along with spectra of a flare is to identify particle acceleration sites, energetics, and the radio/HXR number problem from the combined data sets.

2. OBSERVATIONS

The flare was observed with the Nobeyama Radio Heliograph (NoRH) at 17 and 34 GHz and with RHESSI in hard X-Rays in the energy range 6 – 200 keV. The flare event occurred on 2002 March 14, at 01:43 UT in the active region AR 9866.

The solar active region of interest, crossed the east limb on March 7, and gradually developed magnetic complexity (initially $\beta-\gamma$) as it moved toward the disk center. Intrusive polarity (a δ spot) appeared in its trailing region on March 12, and increased flaring followed in its vicinity. Further magnetic complexity (a second δ) appeared on March 13, and this led to a series of six M-class flares in the following week. The first of this series was an M5.7 flare that occurred at S11E10, peaking at 01:50 in soft X-rays on March 14. This flare was observed in hard X-rays by RHESSI during most of its rise and fall.

In the 10–12 and 12–15 keV bands (Fig. 1) the flare started at 01:37 UT, peaked at 01:47 and continued after 01:54, the beginning of RHESSI night. RHESSI observed three minutes of the late decay phase (02:31-02:34 UT), and in soft X-rays (GOES) the flare continued until at least 04:00. The radio emission was observed from about 01:40 UT and continued beyond 02:00 at which time the level of radio emission was still higher than the pre-flare level.

Late in the flare there is a second peak in flaring emission in both microwaves and HXR, which also shows up as a short duration weak continuum in the Hiraiso dynamic spectra (in the frequency range 30-500 MHz, 01:50-01:57 UT).

3. RHESSI HARD X-RAY OBSERVATIONS

3.1. Time Profiles

The time profiles of the flare in hard X-rays as observed by RHESSI in ten energy bands are shown in Fig 1. During the rise, count rates per detector exceeded 50,000 counts/s (the point at which pulse pile-up becomes significant), and the first attenuator automatically switched in at 01:42:20 UT. This is seen as a discontinuity of the time profiles in the lower energy bands. (The discontinuity has been approximately accounted for in computing the photon rate.)

The X-ray flux in the low energy bands (10–12, 12–15 keV) continued to rise for 3-4 minutes, but in the higher energy bands (24–200 keV), a number of impulsive bursts appeared at a mean cadence of $\sim$1 min, each burst lasting for 30–60 s.

3.2. RHESSI Hard X-ray Imaging Observations

Cleaned images were made in nine energy bands (12–15, 15–19, 19–24, 24–30, 30–37, 37–45, 45–55, 55–75, 75–200 keV) for the period 01:36:00–01:42:00 and 01:42:30–01:54:30 UT. Except for the earliest maps (for 01:36:00–01:39:00), each map was based on 60-s integrations, with 2-arcsec pixels over a field of view (FOV) of $128'' \times 128''$. Fig. 2 shows the inner $90'' \times 90''$ portion of these maps with a dashed line indicating the photospheric neutral line, derived from the MDI magnetogram at 01:36 UT. All map times are start times.

The "pre-flare" source at 01:36 UT (column 1 in Fig. 2) can be mapped only at energies below $\sim$ 19 keV. The source seen in this 3-minute map (01:36–01:39 UT) has a single component, undoubtedly thermal. The first flare image set made during the rise (01:40:00-01:41:00 UT, columns 2 and 3) shows an elongated structure in the 12–15 keV band (feature "A" in Fig. 2), with two compact "footpoint" features at either end, seen best at energies above 30 keV. There is a separate compact source (feature "B" in Fig. 2, column 3) to the southeast of the elongated source on the east side of the neutral line.

In the two minutes following the 19-75 keV peak of the flare, after the attenuator switched in, the southern compact source (feature "B") becomes stronger and then disappears. The highest band that shows mappable sources is 75-200 keV at 01:42:30 UT. The central elongated source (feature "A") breaks up into one or two compact sources at higher energies, fading out at X-ray energies > 55 keV. There is an additional compact source > 15 keV (feature "C" in Fig. 2, 01:42:30, 15-19 keV) which appears to be on the west side of the neutral line, implying that any magnetic flux from the other sources must connect to it.

During the flare, the compact sources, which undoubtedly coincide with magnetic footpoints, move in two different directions, the eastern ones proceeding north, and the western ones moving west. (Fletcher and Hudson, 2002, have analyzed the motions of these footpoints in more detail.) These same footpoints appear to be energized in a second event that peaks at 01:52:10 UT (Fig. 1) and is imaged at energies up to 55-75 keV from 01:50:30 to 01:53:30 (columns 12-14, Fig. 2). At all times, the footpoints appear on or close to the TRACE 195 Å flare ribbons, which appear to spread apart, in the normal manner of flares. Due to counting statistics, the maps from 01:50:00 to 01:50:30 UT show a decrease of map quality with increasing energy. The cutoff above which good maps cannot be made decreases from about 75 keV to 55 keV after 01:43:30.

We were able to make maps at a $4\times$ faster cadence, maintaining image quality by using coarser energy binning. Figure 3 (upper panels) shows 15-s maps made around the peak of the flare in the 12-25 keV band. The figure shows RHESSI contours (dashed) on top of TRACE flare ribbons (white swaths), with MDI background images at 01:36 UT, with positive (white)

and negative (black) magnetic polarity. These maps show that the compact and elongated features have considerable variability on a 15-s timescale. At all times, however, when the image timings are coincident, the RHESSI sources overlie the TRACE ribbons. The converse is not true: the western TRACE ribbon during the rise phase (01:40:00-01:41:45 UT) shows only weak and sporadic HXR emission. After the peak (01:42:30-01:44:15 UT) the RHESSI sources and TRACE ribbons continue to show the association.

The 15-s maps in the 25-50 keV band (Fig. 3, lower panels) show that the flare starts later at higher energies, as can be seen in the multi-band time profiles (Fig. 1). The HXR above 25 keV appear initially at 01:40:30 on the neutral line. In the two 15-s maps at 01:40:30 and 01:40:45 UT showing the onset of > 25 keV X-rays, the flare has first one, then two compact components straddling the neutral line. These compact components appear to be the footpoints of elongated source "A" in the 60-s maps of Fig. 2. After 01:41:00, the 25-50 keV contours become very similar to the 12-25 keV contours. Comparison of the 60-s maps in Fig. 2 with the 15-s maps in Fig. 3 and the 4-s maps of Fletcher and Hudson (2002) indicates that there is some time smearing caused by motions of the sources; it is likely that some of the elongated sources, particularly for $E > 25$ keV), are conglomerates of two or more compact short-lived sources.

4. NORH RADIO OBSERVATIONS

The imaging radio observations were made with the NoRH at 17 and 34 GHz. We also made use of flux monitoring observations with NoRP (Nobeyama Radio Polarimeter) at 1, 2, 3.75, 9.4, and 17 GHz. The NoRP time profiles at these frequencies are shown in Fig. 4. The main radio emission has a rather broad peak at 01:43:40 UT at frequencies 3.75–17 GHz; the emission starts to rise slowly from about 01:42:00 UT. Note, however, that at 1 GHz there is a sharp peak at about 01:42:25 UT, with a correspondingly sharp rise of emission from 01:42:15 UT; the emission with the broader peak (at 01:45 – 01:47 UT) starts to rise at 01:42–01:43 UT. This sharp peak at 1 GHz does not have any counterparts at higher frequencies. The figure shows that the broader peak at around 01:43:20–01:43:40 drifts to later times with decreasing frequency. The main flare emission including another significant peak at 01:52:30 UT lasts only about 15 min. In Fig. 4 we show some RHESSI count-rate time profiles in the 6–12, 12–25, 25–50, and 50–100 keV bands.

We studied the EUV and photospheric relations to the radio components of the flare. Fig. 5 shows a TRACE 195 Å image with MDI and 17-GHz contours at 01:41:43, 01:36:01 and 01:41:46 UT (respectively). One sees the flare ribbons in the TRACE image, and a radio loop-like feature along the neutral line of the magnetic field in the flaring active region.

Investigation of the MDI images near the main flare site shows the appearance of an opposite-polarity delta region at the site, but it does not seem to be directly related to the triggering of the remote flaring, if we consider the flaring loop configuration based upon radio data (see below).

Fig. 6 shows the low level 17-GHz intensity in the late flare phase (01:49:26 UT) along with the RHESSI main flare, superposed on TRACE 195 Å negative images. The radio contours show a "double loop" system configuration of the flare, similar to what we observed in the case of the flare of Oct. 25, 1999 referred to earlier. This configuration consists of a compact bipolar main flare site and a remote site observed to be unipolar in radio. The remote site is weak or nonexistent in HXR, as we describe in the next section.

The TRACE images in Fig. 6 show brightenings (see crosses) appearing progressively farther west between the main and the remote sources. Between 01:42:29 and 01:43:30, the brightest EUV pixel west of the flare moves systematically westward with a mean speed of 210 ± 50 km/s. The radio contours (dashed) seem to follow this motion. This suggests that a disturbance travels from the flare site towards the remote site, and suggests also that the lowest contours of the 17-GHz maps outline a large scale structure. It is probable that this is associated with the surge-filament event seen at Hida Observatory at this time (Kurokawa, private communication). In Figure 7 we present a set of main flare site TRACE images overlain with 17-GHz polarization contours. During the main phase of the flare (from 01:41 to 01:50 UT) one can see the double ribbon flare structure on the TRACE images, with positive polarity over the eastern ribbon and negative polarity over the western one. At later phases of the event we observed the development of the multi-loop complex. On these images the left and right polarization maxima correspond to the positive and negative polarities of the magnetograms.

5. COMPARISON OF RHESSI HXR AND NORH MICROWAVE IMAGES

In section 3 above, we discussed the flare maps obtained by RHESSI. Figure 8 shows MDI images of the main flare site with superposed 17-GHz contours (white) and RHESSI HXR contours (black) in the energy ranges from 12 keV to 200 keV at 01:42:00 UT (start time). These contours represent X-ray emission during the maximum phase of the event. As one can see, at the main flare phase the 12–15 keV contours correspond to the loop-top emission and they have good agreement with the 17-GHz contours. The lower contours of the 15–19 keV, 19–24 keV sources correspond to the emission of the elongated loop system with a general SE-NW orientation. Going higher in energy we begin to see emission from the footpoints of the main flaring arcade. The higher energy contours mostly represent emission

from the main flare footpoints. The 17-GHz contours lie between the RHESSI foot points. This implies that the microwave emitting electrons (which are of higher energy than the HXR emitting electrons) fill up the main flaring loop with the foot points emitting only HXR emission. A component seen at this time located near (-400,-100) in the energy range 12–50 keV seems to correspond approximately in time to the spiky source at 1 GHz (Fig. 4, 01:42:10-01:43:00, peaking at 01:42:20). This is component "B" in Fig. 2. The 15-s HXR maps (Fig. 3) show that this source appears at 01:40:30-01:40:45 at 12-25 keV, and 01:41:00-01:41:15 at 25-50 keV, preceding the onset of the spiky 1-GHz peak by 60-90s, and disappears at 01:43:15-01:43:30 in both the 12-25 and 25-50 keV bands, 15-30s after the decay of the 1-GHz event. The events in the two domains overlap in time, and the delay of the radio source is similar to the other radio delays relative to HXR in this flare, so it is possible that the HXR and 1-GHz events are associated.

The RHESSI Clean maps show only a small enhancement in the region of the remote source (see Fig. 9). There are two minor maxima near one of the TRACE 195 Å features in the remote region at 01:43:11, close to the time of the maximum 17-GHz remote component. To show this weak source, we made a 1-min Clean map at 12-25 keV using the subcollimators coarser than 12″ to minimize over resolution, placing the main flare in the corner of the field so that phase smearing would slightly smear out its brightness contribution. Only one source in the remote system appears with a contour above the 5% level. This source, which may possibly be a sidelobe artifact, contains about 1.8% of the total flux in the map. Thus if there is a HXR remote source, it is a very weak one.

Figure 10 shows an MDI magnetogram and 17-GHz V images and RHESSI contours at four different times (01:37:51, 01:42:30, 01:43:30, and 01:52:30 UT). The first time is pre-flare, and the next two correspond to times during the main flare peak. The last one corresponds to the time of the peak during the later phase of the event. One can visualize several different loop systems being involved in the flare process. One should note that at the time of the later peak (01:52:30 UT), each of the higher energy (50–100 keV) footpoints is located at one polarity (positive and negative) of the 17-GHz polarized emission. This obviously defines one flaring arcade. At 01:42:30 and 01:43:30 UT, one sees the same phenomenon, namely each of the footpoints in the energy channel 50–100 keV overlies (to within 10″) one polarity of the 17-GHz polarized emission, but this polarity is located south of the previous 17-GHz positive polarity position. This defines the second flaring arcade. Then there is the larger source emitting 12–25 keV HXR without any well-defined footpoints, and the two end points extend slightly beyond the previous RHESSI footpoints. Since the extension is less than half the RHESSI resolution (13″) used for this comparison, the difference is not significant. A possible loop footpoint is suggested by the discrete SE source (feature "B" in Fig. 2) near (-400,-100).

Using the NoRH maps of the flare we calculated the time profiles of the radio flux at 17 and 34 GHz separately for the main and remote sources. Figure 11 shows time plots of intensity and polarization for the main and the remote sources. The remote source shows a time delay of $\sim$ 30s relative to the main source. Fig. 12 shows for the main source 17- and 34-GHz brightness temperature time profiles along with the derived spectral index. Analysis of the profiles under the assumption of a uniform source might suggest that the main source has mostly thermal emission near the minima of the index. But many of the lowest values occur on the declining side of the main peak, as well as in the minima, and if the sources are as non-uniform as the images indicate, the flatter spectral index could be due to the superposition of two or more gyrosynchrotron sources of different magnetic field strengths. (For example, the spectrum of one might peak near 17 GHz, and the spectrum of the other several GHz higher.) Both the main and the remote source have nonthermal emission, as implied by the polarization (left circular polarization $\sim$ 60% for the remote source), the impulsive variations (on time scales ¡ 10 s for the remote source), and brightness temperature ($>> 10^7$ K for the main source). As we have noted, the HXR emission in the remote region is weak or non-existent.

The main source has bipolar structure and so we present the time profiles of 17-GHz radio emission separately for the left and right circular polarities (Fig. 13). The western side of the main source is left–circularly polarized with polarization degree of about 30%. This source represents mostly radio emission from the flaring loop footpoint. According to MDI images it is located above a sunspot. The eastern side of the main source is right-circularly polarized with a polarization degree of $\sim$ 10%. The radio emission mostly originates from the eastern part of the main source (Fig. 13).

In contrast with the clear $8 - 12''$ motion of the RHESSI footpoints, the 17-GHz polarization images of the flaring source do not show unequivocal motions, but this may be the result of relatively lower spatial resolution at 17 GHz ($\sim 10''$) as compared with the best RHESSI resolution ($6.9''$). However, comparison of earlier and later V maps (e.g. Fig. 10) does show that the eastern V component appears to move north by $\sim 10''$ with the associated HXR component between 01:43:30 and 01:52:30 UT.

6. HARD X-RAY SPECTROSCOPY – RHESSI DATA

Spectroscopy using the Solar Software's "SPEX" (Schwartz *et al.* 2002) permitted us to make multi-parameter fits of a thick-target model to the photon spectra: temperature and emission measure of the thermal component, and flux and slope(s) of the nonthermal components(s) of the electron energy distribution. The fits to the photon spectra for one

model using a single thermal component and a double nonthermal component are shown in Fig. 14 for the period 01:42:30–01:53:50.

The crosses show the background-subtracted data with error bars in flux and energy bandwidth. The triangles show the background that was subtracted. The solid line shows the power-law components and the line with dots shows the thermal component. The background has been subtracted, but its contribution is significant only above ~ 50 keV.

For the purposes of this analysis, the background in each energy band was taken to be constant, equal to the mean pre-flare count rate in the 01:14–01:18 time range.

The model used to fit the data is an isothermal plus broken power-law electron distribution with lower and upper cutoffs. The model, described by Holman (2001), Holman *et al.* (2003), is determined by computing thick-target bremsstrahlung from a multi-parameter distribution in 20-s time bins throughout the flare. This kind of electron-based model is preferable to photon spectral modeling because it is one step closer to the acceleration physics.

The initial model has 8 parameters: emission measure (EM), temperature (T), thick-target electron flux (a_{norm}), power-law indices (δ_1, δ_2) above and below the energy break E_{brk}, and lower and upper cutoffs (a_{co}, b_{co}). Fits made with all 8 parameters show that the upper index $\delta_2 > 5$, meaning that the fits should be only marginally affected by the upper cutoff. Only a lower limit on b_{co} can be found: $b_{co} \sim 400$ keV, and in subsequent fits we have fixed b_{co} at this value. The break energy E_{brk} is not well determined throughout the flare. We have therefore taken the break energy to be constant at 40 keV. The resultant fits with 6 free parameters are not significantly different in quality as measured by the χ^2 statistic. We have tried fits without a nonthermal break (4-parameter fits), and find poor fits. This indicates that the break energy is a real property of the electron distribution.

In general, the lower cutoff, which is crucial for the determination of total nonthermal energy, does not show significantly smaller χ^2 when it is changed from 10 to 20 keV. We have therefore done 5-parameter fits (2 thermal and 3 nonthermal) for lower cutoffs of 10 and 20 keV. The χ^2 statistic is less than 1 for all time intervals with either cutoff. The time dependencies of the parameters are shown in Fig. 15, to be discussed in the next section.

In the next section we discuss the HXR thermal/nonthermal and HXR/radio electron number problems based on our model. It is possible that other more complicated models of the thermal component could fit the data equally well, but they would not change our estimates of electron numbers or the energetics significantly. The degree of non-uniqueness of inverting bremsstrahlung spectra has been discussed by Brown and Emslie (1988) and Holman, (2003).

7. DISCUSSION

We have observed a flare of importance M5.7 using RHESSI in hard X-rays and NoRH at 17 and 34 GHz simultaneously. The flaring source in microwaves clearly exhibits a "double loop" configuration similar to what we observed for a flare on October 25, 1999 and several other flares (Kundu *et al.* 2001, Kundu and Garaimov 2003). At the main flare site the microwave source has two distinct oppositely-polarized components, which must delineate a small loop. The remote source which is connected to the main flare site by a large loop system seen unequivocally only in radio, is most likely due to a stronger magnetic field. Even with RHESSI's high sensitivity one does not clearly observe HXR at the remote site. A weak HXR source mapped in the vicinity of the remote microwave source has $< 2\%$ of the flux of the main source at 12-25 keV.

The RHESSI HXR sources consist of several evolving loops. Around the peak of the flare (01:41:00-01:43:30) there is one elongated feature almost parallel to the flare ribbons ("A" in Fig 2) seen predominantly at lower energies. This feature shows HXR footpoints on either side of the neutral line at energies > 45 keV. At the same time, there are two other footpoint sources ("B" and "C" in Fig. 2) beyond the north and south ends of this source, seen at energies from 12-37 keV, and lying on opposite sides of the neutral line, suggesting another loop which overlies the first. The 17-GHz V maps (Figs 7 and 10) show oppositely-polarized sources also straddling the neutral line, close in position to the ends of the elongated HXR feature "A". The 17-GHz I maps (Figs 5 and 8) show that most of the microwave emission occurs between the oppositely-polarized footpoints, which suggests that microwave emitting electrons must fill up most of the loop. Note that during the impulsive peaks the microwave emission is mostly produced by higher energy electrons via the gyrosynchrotron mechanism, whereas the hard X-ray emission is produced by bremsstrahlung from both thermal and power-law sources.

Some of the microwave emission may be thermal, but without images at more closely spaced frequencies it is difficult to determine the fraction of thermal emission from the radio observations alone; but the emission measure of the thermal component determined from HXR spectroscopy can show whether it is optically thin.

It is of interest to compare the components of the electron spectra fitted to the RHESSI HXR data, but it is not feasible to make images that distinguish the spatial features of each component at all energies and at all times. However, isolated images in Fig. 2 show the main features of each component. Inspection of the spectral fits (Fig. 14) reveals that in certain bands and time ranges, only a single component dominates. Using these model fits, we have identified the time intervals and bands during which one component radiates $\geq 90\%$ of the total band flux. The thermal component morphology is shown by the 12–15 keV

maps (Fig. 2) for 01:36-01:39 and 01:43:30–01:53:30 UT, and 12–25 keV maps (Fig. 3) for 01:41:00-01:41:45 UT, where the elongated "A" source dominates the flux. The nonthermal component is shown by the maps for 37 keV and higher in the same time period.

We do not find evidence in this flare for coronal thick target emission. In all of the 1-min maps (Fig. 2), with the exception of the maps starting at 01:41 UT, the loop-like features appear in energy bands ¡ 30 keV, and are most likely thermal. However, in the case of the 01:41 maps (Fig. 2), a "looplike" feature appears in the 30-37 keV band. In the higher cadence maps (15-s maps in Fig 3 and Fletcher & Hudson's 4-s maps in their Fig. 6) show that the "loop-like" sources break up into compact footpoint-like features. This indicates that there is some time smearing of the moving footpoints. The exceptions shown in Fig. 3b at 01:41:00-01:41:15 and 01:41:30-01:41:45 UT show changes on a 15s timescale– the apparent "loop" breaks up into 2 compact components in the 01:41:15-01:41:30 map. Furthermore, since the 25-50 keV band is dominated (60spectrum, any "loop-like" structure in that band is probably due to the thermal component. Fletcher and Hudson's 4-s maps suffer from the problem that they are in the 20-30 keV band, where thermal structures contribute significantly. We conclude that throughout the flare, the emission was dominated by thick-target chromospheric sources. This is consistent with the radio and HXR spectral observations, which suggest that there are different electron populations for radio (trapped) and HXR (precipitating). It is unlikely that in this flare the HXR loops are sufficiently dense for coronal thick targets above 30 keV, although evidence for such dense loops does exist in other flares (Veronig and Brown, 2004). The electron column density required to stop 30 keV electrons is about 1×10^20 cm^{-2} scaling as E^2, and this is more than an order of magnitude higher than we infer from our thick-target model, again consistent with compact chromospheric components.

We have used our model to determine the thick-target electron flux $\Phi(E,t)$. Integrating the loss rate $\Phi(E,t)$ over energy from the lower cutoff (estimated to lie in the 10-20 keV range), we get the rate of electron loss, $P(t)$, in the target. Actually, the lower and upper cutoffs are not well determined (see Fig. 15a). As mentioned above, we therefore use the two limits, 10 & 20 keV, for the lower cutoff, and 400 keV for the upper cutoff. The latter is where the precipitating electrons radiate 200 keV photons, the upper limit of photon energies with spectral information.

Fig. 15b shows the computed electron loss rate $\Phi(t)$ for the two selected lower cutoffs; for 10 keV, $\Phi(t)$ ranges over $2 \times 10^{36-38}$ electrons/s, and for 20 keV, $\Phi(t)$ ranges over $2 \times 10^{35-36}$ electrons/s. The number of nonthermal electrons $\int \Phi(t)dt$ is shown in the upper part of the same panel. It asymptotically reaches 5×10^{40} electrons for the lower cutoff, and 8×10^{38} electrons for the higher cutoff.

The energy distribution loss rate $P(E,t)$ is computed from $\Phi(E,t) \cdot E$, and the energy loss rate $P(t)$ is found by energy integration. These are shown in Fig. 15c. For the two cutoffs, 10 & 20 keV, the integrated electron loss is 4×10^{32} ergs and 1×10^{31} ergs, respectively.

The total number of thermal electrons is computed from the emission measure EM (cm^{-3}) (Fig. 15d) and inferred source volume $V(cm^3)$: $N_{therm} = \sqrt{(EM/Vq)}$. where q is the fill-factor, assumed to be unity. From the maps, we estimate V= 8.8×10^{26} cm^3. Given EM = 2×10^{49} cm^{-3}, we find $N_{therm} \geq 1.3 \times 10^{38}$ electrons ($q \leq 1$). This is of the same order as the total number of nonthermal thick-target electrons estimated from our model assuming a 20-keV energy cutoff, $N_{NT} = 8 \times 10^{38}$ electrons. With a 10-keV cutoff, N_{NT} is about 2 orders of magnitude higher, while the thermal source remains about the same.

The total thermal energy from the RHESSI data is found using EM as above, and $T = 2.6 \times 10^7$ K (2.2 keV), as shown in Fig 15e. This is $3kT\sqrt{\mathrm{EM} \cdot \mathrm{V}} = 1.4 \times 10^{30}$ erg, where k is Boltzmann's constant, 1.38×10^{-16} erg/deg. (The thermal energy derived from the GOES data is about 20% higher.) This is about an order of magnitude smaller than the estimate of the time- and energy-integrated electron loss for a 20-keV lower cutoff, exhibiting the well-known excess of the nonthermal energy over the inferred thermal energy (Dennis *et al.* 2003, Holman *et al.* 2003).

It is of interest to compare the HXR numbers with those inferred from the radio observations. The upper electron spectral index inferred from hard X-rays is $\delta \sim 5.5$ (Fig. 15f). We assume that this spectral index is the same at MeV energies, where electrons contribute most of the gyrosynchrotron emission. If the source is optically thin at 17 and 3 GHz, as suggested by the fact that the total flux density decreases between 9.4 GHz and 17 GHz (Fig. 4.), then the brightness temperature is proportional to the emissivity η_ν (erg cm^{-3} s^{-1} Hz^{-1} $ster^{-1}$): $T_b = (c^2/k\nu^2)\eta_\nu L$. We assume that the radiating volumes are identical in hard X-rays and microwaves, and that $L \sim 5 \times 10^8$ cm, so that $T_b = 1.1 \times 10^{25}$ η_ν at 17 GHz. From Dulk and Marsh (1982), we estimate the dependence of η_ν on magnetic field B (gauss), density N (cm^{-3}), δ and frequency ν (Hz). The nonthermal electron density is 2×10^9 cm^{-3} in the first minute of the flare, given the volume used earlier, and a 20-keV cutoff. (For the 10 keV cutoff it is 10 times higher.) At frequencies much greater than the gyrofrequency, and with $\delta = 5.5$, Dulk and Marsh's expressions yield $\eta_\nu = 1.5 \times 10^{-27} BN(\nu/\nu_B)^{-3.73}$ where we have assumed that the angle relative to the magnetic field is 45°, and the gyrofrequency ν_B (Hz) $= 2.8 \times 10^6$ B (G).

If the source is uniform, the magnetic field necessary to match hard X-rays and radio at the start of the flare, when $T_b(\nu = 17\ \mathrm{GHz}) = 8 \times 10^7$ K, would be $\sim 1 \times 10^3$ G. At such field strengths, $\nu_B \approx \nu/6$, still in the Dulk & Marsh domain, but $\nu_{peak} \approx \nu$, which contradicts the observed decline of the peak total flux from 9.4 to 17 and to 34 GHz (1450, 900 and 580 sfu

respectively), so the assumption of a uniform source may be inaccurate.

Fig. 12 shows the Nobeyama brightness temperatures as a function of time in the flare. At the onset of the microwave flare (01:41:50), the 17/34-GHz spectral index is ~ 2.7. For most of the main burst, during the rise to maximum at 01:43:30, and during the decay to 01:45:30, just before a secondary burst, the spectrum continuously hardens. This is what has been termed a "soft-hard-harder" (SHH) behavior, more commonly seen in microwaves than in HXR (Silva, Wang, and Gary, 2000). In this flare the SHH behavior is not seen in the RHESSI spectra. Indeed (as shown in Fig. 15), the spectrum below 40 keV softens during this interval, and the spectrum above 40 keV remains nearly constant in slope. Three possible explanations for the SSH behavior have been given in the literature: 1) Continued acceleration of the electrons to energies (> 300 keV) where they strongly radiate microwaves; 2) Second-step acceleration; 3) Trapping of the electrons in a magnetic loop.

The difference between the values of the radio and HXR indices argues against (1): the HXR index is always > 5 at the highest accessible RHESSI energy band (75-200 keV), while the microwave T_b spectral index is always < 3. (The flux spectral index is a little higher, but always less than 3.5.) Since the radio and HXRs are presumed in (1) to have a common origin, they would have to have the same inferred electron spectral index, and here they do not. (See also Silva et al. for other examples.) As for possibility (2), the smoothness of the hardening spectrum argues against a second step in acceleration. The remaining explanation (3) is consistent with the images, which show precipitation sites in HXR above 37 keV (Figs. 2 and 8), while the 17-GHz maps show extended sources between the footpoints (Fig. 8), where the trapped electrons radiate by the gyrosynchrotron mechanism.

As shown in Fig. 12, throughout the flare the 17/34 GHz brightness temperature index is less than 3, which, in turn, is less than the mean electron spectral index of 5.5 inferred from HXR (Fig 15f), so smaller magnetic fields (a few $\times 10^2$ G) would suffice to explain the nonthermal part of the radio flux, and the density of the microwave-emitting electrons may be orders of magnitude smaller than the bulk of the HXR-emitting electrons.

The flat 17/34 GHz T_b spectrum is not explained in terms of a thermal radio source, because that would conflict strongly with the HXR emission measures ($< 2 \times 10^{49} \mathrm{cm}^{-3}$) and temperatures ($< 3 \times 10^7$K). The minimum emission measure required to make the thermal source optically thick ($\tau_{17} > 1$) is 2×10^{51} cm^{-3} for a temperature of 40×10^7K at the 01:44 minimum in the spectral index shown in Fig. 12. Thus the flattening must be interpreted in terms of nonuniform magnetic fields, whose character is poorly constrained by the spectral observations.

The number of microwave-emitting electrons required to match the HXR-emitting elec-

trons (cf. earlier discussion) seems to require unrealistically large magnetic fields. But this objection becomes moot if the bulk of the HXR come from the footpoints, and the microwaves come from the loop bridging the footpoints.

8. CONCLUSIONS

We have found evidence that the HXR low energy source (< 19 keV) agrees in size and location with the 17-GHz source, but the high energy (> 37 keV) sources appear as footpoints at the extremes of the 17-GHz source. At the peak of the flare, the 17-GHz source encompasses most, but not all, of the loop implied by the HXR footpoints at energies > 37 keV. This is consistent with a trap + precipitation model for 17 GHz and HXR (respectively), as first suggested by Melrose and Brown (1976) for UV and HXR and later by Raulin et al. (1999) to explain the delay of the radio peak relative to HXR. The soft-hard-harder behavior of the radio spectrum during the main impulsive burst is consistent with the picture of increased trapping of high-energy (> 300 keV) electrons radiating via the gyrosynchrotron mechanism while lower energy (< 200 keV) electrons precipitate at footpoints that radiate 37-200 keV X-rays.

The multiple structures imaged here in both radio and hard X-rays indicate that the coronal magnetic field may be quite nonuniform, and thus the inferred flatness of the spectrum (9-34 GHz) may simply be due to the superposition of more than one gyrosynchrotron source, one with a spectral maximum close to 17 GHz and another with maximum several GHz higher. More closely-spaced multi-frequency imaging is necessary to resolve this issue.

We have found that there are several magnetic loop systems in the flare, at least one of which is not, or only weakly, seen in hard X-rays. The low energy HXR sources consist of at least two loop systems with footpoints spanning the neutral line, and these are energized progressively during the flare. This part of the flare may have been triggered locally by the appearance of "δ" magnetic fields.

In addition to oppositely-polarized footpoints and arcades associated with the $10 - 19$ keV HXR sources, the radio observations show a long structure extending to a "remote source" over the western sunspot of the region. This remote brightening may have been triggered by a more global process than the main flare. During the brightening of the radio remote source, whose time profile closely resembles that of the main source with a delay of ~ 30s, there was progressively westward brightening of EUV 195 Å features with an activation speed of ~ 210 km/s. This speed is below the usual range of shock waves, but is more typical of surges. In fact, a surge/filament event was seen in Hα at Hida observatory, starting at 01:41 UT, close

to this location (Kurokawa, private communication). The fact that the radio contours seem to move with the the EUV brightenings (Fig. 6, lower panels) may imply that electrons are energized by the passage of the disturbance and that they produce gyrosynchrotron emission in the weaker fields expected far from sunspots, or possibly spatially-extended, optically-thin, free-free emission from heated loops of temperatures a few times 10^6 K. The appearance of the remote source in radio near the western spot group along with minimal or absent HXR may be simply the result of stronger coronal magnetic fields in the remote region. A similar explanation has been used to account for the asymmetries often observed in double footpoint HXR/microwave flares (Kundu et al, 1995, Wang et al 1995).

In the main flare, the formation of new loops seems to follow a pattern in which magnetic loops, as inferred by their moving HXR footpoints, become less parallel to the flare ribbons and more oriented perpendicular to them. Such a pattern has been seen in other flare observations by HXT, where motion of HXR footpoints suggested that the magnetic loops went from a highly sheared state to a less sheared state during the course of the flare (Masuda, Kosugi, and Hudson, 2001, Somov et al, 2002). Somov *et al.* interpret this behavior as the result of relaxation of magnetic tension generated by photospheric shear flows.

9. ACKNOWLEDGMENTS

The research at the University of Maryland was supported by NASA grants NAG 5-12860 and NNG 04 GG 33G and by NSF grant ATM0233907. The work of EJS was supported by NASA grant NAG 5-10180. The authors thank Linhui Sui for helpful discussions.

REFERENCES

Brown, J., & Emslie, A.G.: ApJ **331**, 554, 1988.

Dennis, B., Veronig, A., Schwartz, R., Sui, L., Tolbert, A., Zarro, D. & the RHESSI Team: Adv. Spa. Res. **32**, No. 12, 2459, 2003.

Dulk, G. & Marsh, K.: Sol. Phys. **111**, 113, 1982.

Fletcher, L., and Hudson, H. S.: Sol. Phys. **210**, 307, 2002.

Hanaoka, Y.: ApJ **420**, 37, 1994.

Hanaoka, Y.: Sol. Phys. **165**, 275, 1996.

Hanaoka, Y.: Sol. Phys. **173**, 319, 1997.

Hanaoka, Y.: in Nobeyama Symp., Solar Physics with Radio Observations, eds. T. Bastian, N. Gopalswamy & K. Shibasaki (Tokyo: Nobeyama Radio Obs.), 229, 1999.

Holman, G.: http://hesperia.gsfc.nasa.gov/hessi/flarecode/bremthickdoc.pdf, 2001.

Holman, G.: ApJ **586**, 606, 2003.

Holman, G., Sui, L., Schwartz, R. & Emslie, G. A.: ApJ **595** L97, 2003.

Inda-Koide, M., Sakai, J., Kosugi, T., Sakao, T., & Shimizu, T.: PASJ**47**, 323, 1995.

Kundu, M. R., Grechnev, V., Garaimov, V., & White, S.: ApJ **563**, 389, 2001.

Kundu, M. R. & Garaimov, V.: Adv. Spa. Res. **32**, No. 12, 2497, 2003

Kundu, M. R.; Schmahl, E. J.; Velusamy, T.: ApJ **253**, 963, 1982.

Kundu, M., Nitta, N., White, S., et al.: ApJ **454**, 522-530, 1995.

Kundu, M. R. & Shevgaonkar, R.: ApJ **297**, 644, 1985.

Kurokawa, H.: Space Sci. Rev. **51**, 49-84. Oct. 1989.

Masuda, S., Kosugi, T., & Hudson, H.: Sol. Phys. **204**, 55, 2001.

Melrose, D., and Brown, J.: MNRAS **176**, 15, 1976.

Raulin, R., White, S., Kundu, M., Silva, A., and Shibasaki, K: ApJ **522**, 547, 1999.

Schwartz, R., Csillaghy, A., Tolbert, A., Hurford, G., McTiernan, J., Zarro, D.: Sol. Phys. **210**, 165, 2002.

Silva, A., Wang, H., & Gary, D.: ApJ **545**, 1116. 2000.

Shimuzu, T., Tsuneta, S., Acton, L., Lemen, J., Ogarwara, Y., & Uchida, Y.: ApJ **422**, 906, 1994.

Somov, B., Kosugi, T., Hudson, H., Sakao, T., & Masuda, S.: ApJ **579**, 863, 2002.

Veronig, A.M, and Brown, J.C., Adv. Spa. Research, **35**, Iss. 10, 1683-1689, 2004.

Wang, H., Gary, D. E., Zirin, H., Schwartz, R. A., Sakao, T., Kosugi, T., Shibata, K.: ApJ **453**, 505-510, 1995.

Zirin, H.: ApJ **274**, 900, 1983.

This preprint was prepared with the AAS LaTeX macros v5.0.

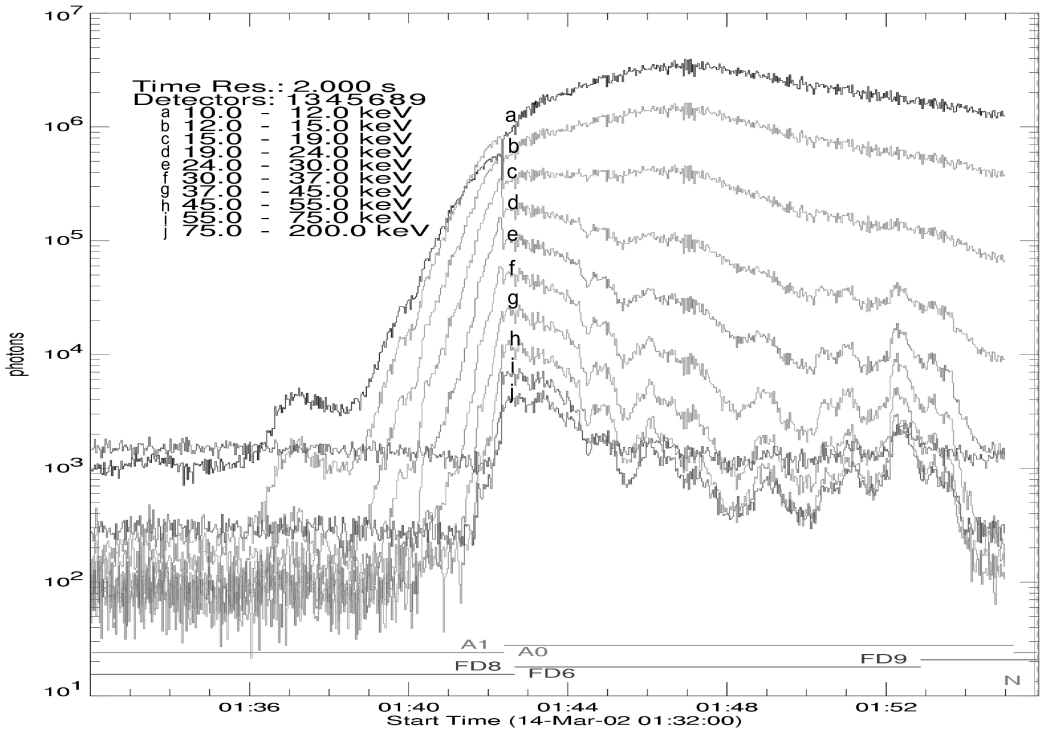

Fig. 1.— Time profiles of RHESSI hard X-rays in 10 energy bands spanning photon energies from 10 to 200 keV. There is a short discontinuity starting at 01:42:20 UT when the thin attenuator switched in to prevent pulse pileup at low energies.

Fig. 2.— RHESSI narrow-band images of the flare. The 15 columns show Cleaned maps over a $90'' \times 90''$ field of view, centered at heliographic (-375,-75), with $2''$ pixels. The contours at lower energies are at 40, 60, 80 and 99% of the map maximum. At higher energies where noise is significant, lower contours are deleted for clarity. The times at the top of each column represent the start time (UT) of integration. With the exception of the first map (for 01:36:00-01:39:00), the maps were made using 60 s of integration starting at the indicated times. The dashed line shows the photospheric neutral line derived from MDI magnetograms. Components labeled A, B and C are discussed in the text.

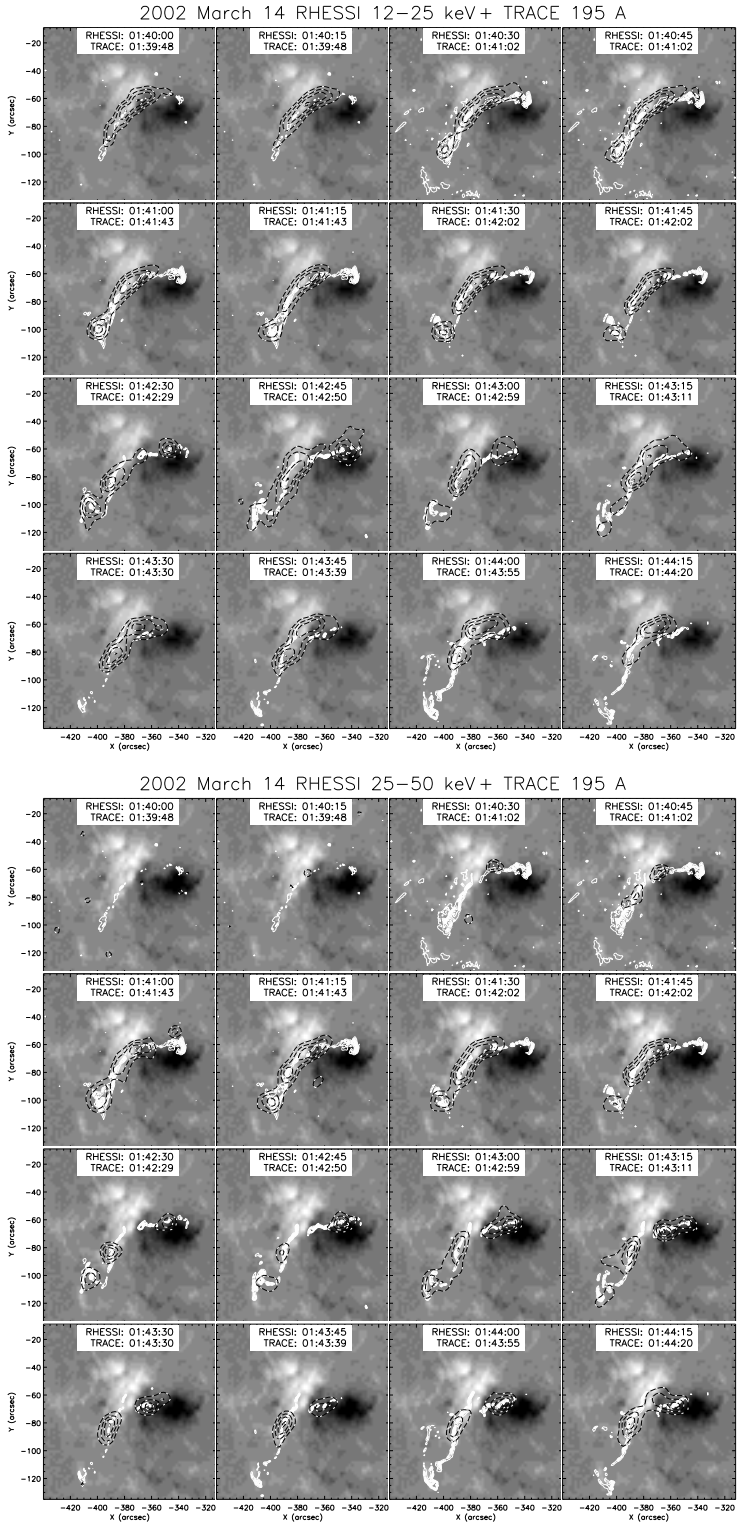

Fig. 3.— Top panels: RHESSI Cleaned maps made with a 15-s cadence from 01:40:00 to 01:44:15. The dashed contours (40,60,80,99%) are for 12-25 keV X-rays, and the grey scale background shows the longitudinal magnetic field from MDI at 01:36 UT. (light=positive, dark=negative). The TRACE 195 Å flare ribbons are shown as bright swaths along the neutral line. Lower panels: Same as top but for 25-50 keV.

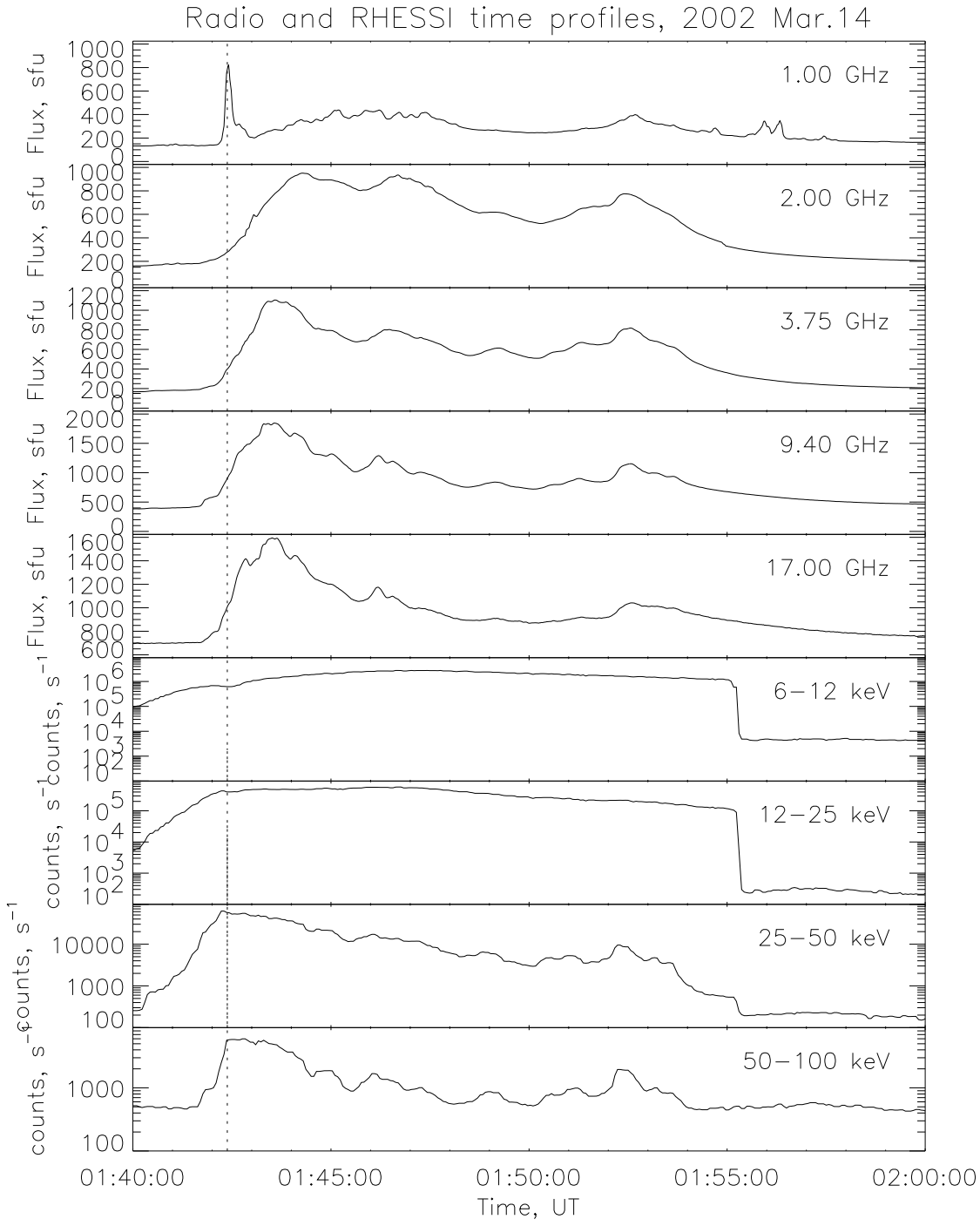

Fig. 4.— Time profiles of the total flux from the Nobeyama polarimeter and heliograph and the RHESSI HXR count rate

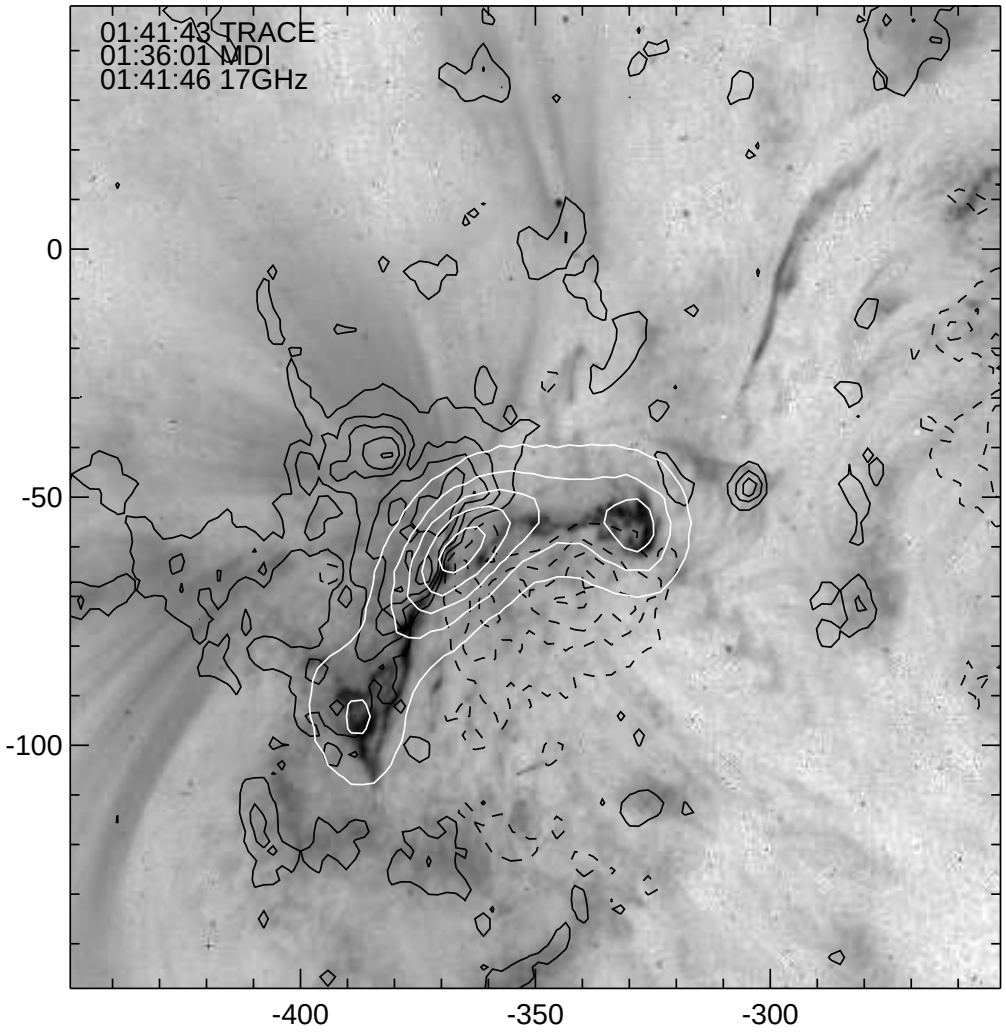

Fig. 5.— TRACE 195 Å image (negative) with MDI contours (black: -90 to 90% of maximum in steps of 20%) and 17-GHz contours (white: 10,30,50,70,90%)) around 01:41 UT, with start times specified in the figure. The two bright flare ribbons appear in regions of opposite magnetic polarity. A radio loop-like feature bridges the neutral line, and two compact components overlie the ribbons in opposite polarities of the photospheric magnetic field.

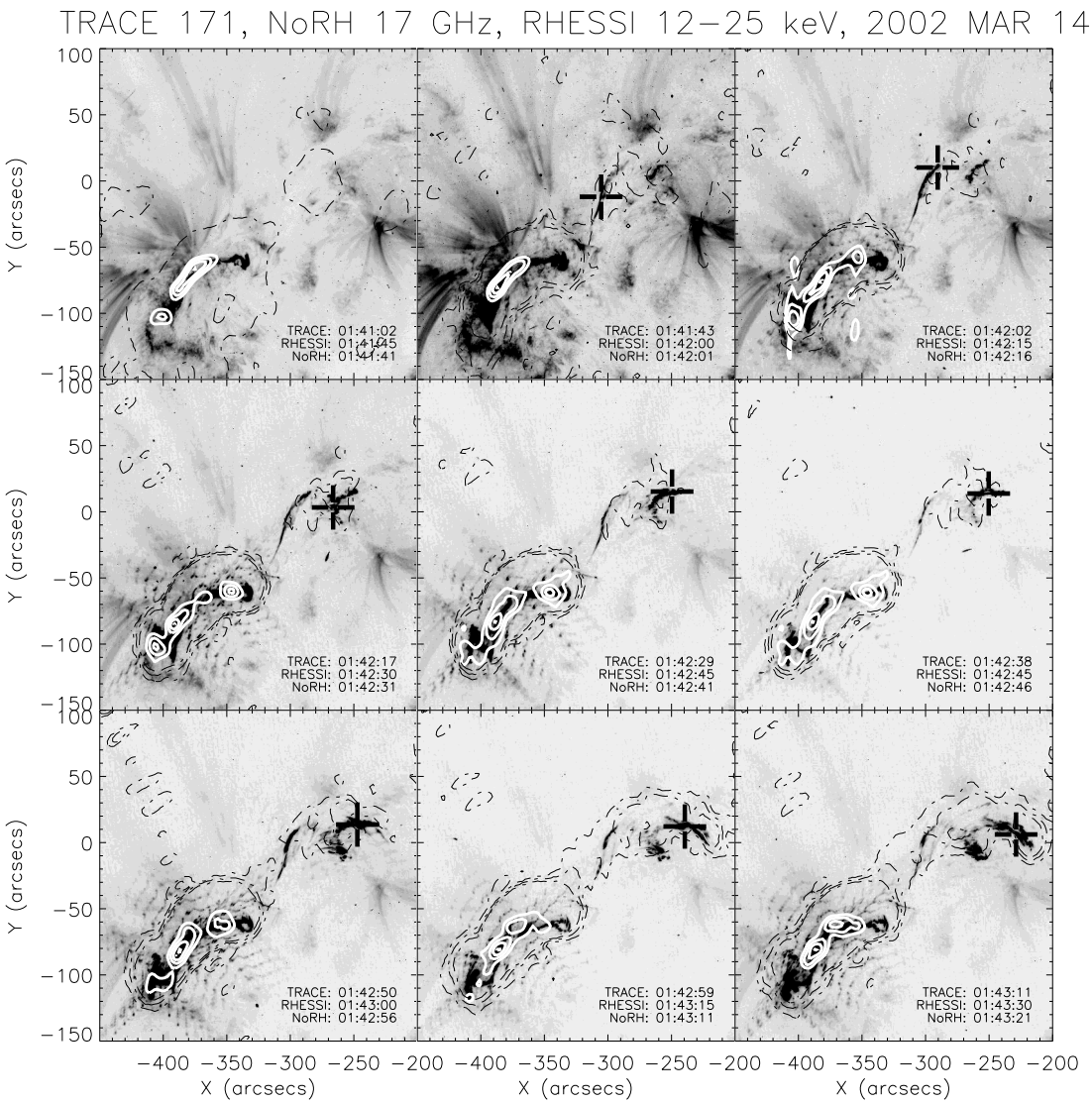

Fig. 6.— 17-GHz Intensity and RHESSI 12-25 keV HXR superposed on TRACE Å images. Dashed black contours (0.1,0.2,0.4% of maximum) show the lower levels of 17-GHz intensity. White contours (41,60,80,99%) show the RHESSI 12-25 keV HXR from the main flare. The negative greyscales show TRACE 195 Å images from 01:41:02 to 01:43:11 (start times) with progressive brightening of coronal material between the main source and the remote source. From 01:41:43 to 01:43:30 the successive brightenings, marked by crosses, appear steadily further west within the boundaries of the lowest 17-GHz contour.

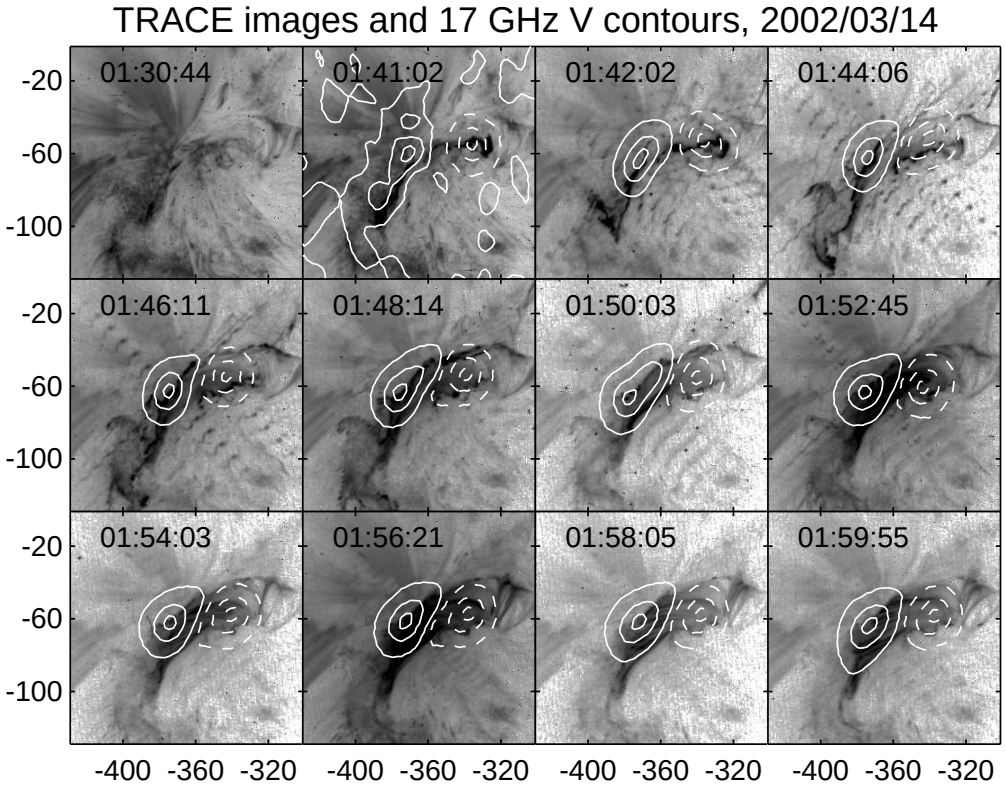

Fig. 7.— TRACE 195 Å images and 17-GHz V contours at 10, 50 and 90% of local maximum (solid–positive; dashed–negative). The times in the figures specify the start times of 5-s maps.

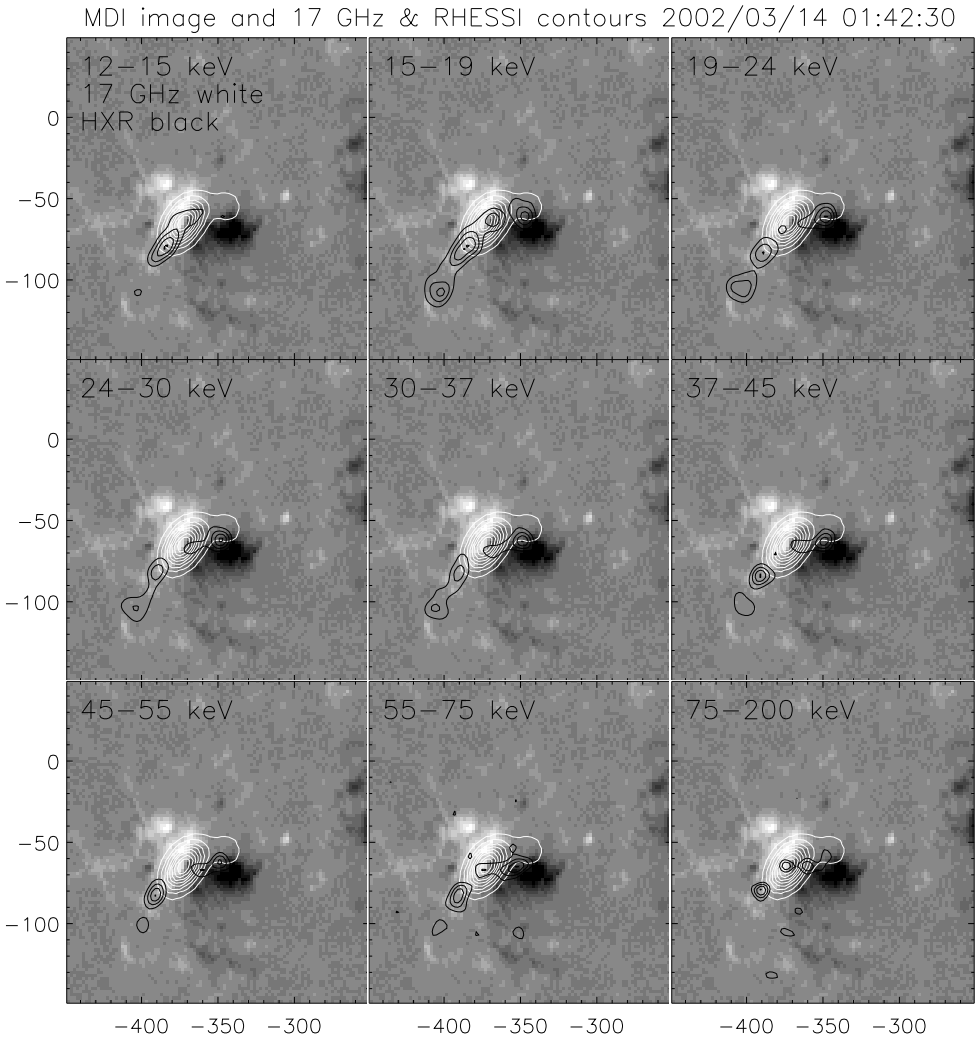

Fig. 8.— MDI magnetogram with superposed 17-GHz contours (white, 10,30,50,70,90%) and RHESSI HXR contours (black, 40, 60, 80, 99%). The HXR maps are for the 01:42:30-01:43:30 interval, and the 17-GHz maps are for 01:42:31-01:42:36 UT.

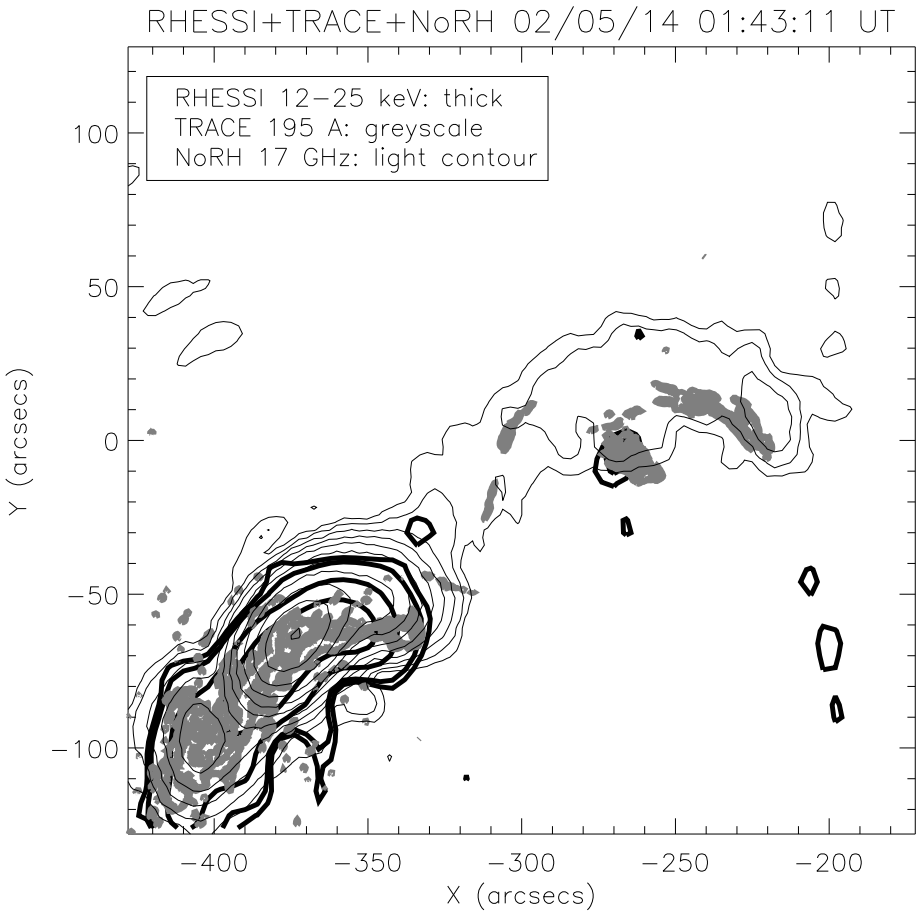

Fig. 9.— The remote source region in microwaves (contours=max/2^n, n=0 to 10), EUV, and HXR at 12-25 keV (contours=3,6,12,25%) in the 01:43-01:44 UT time period. The HXR map center has been shifted to move the main source to the corner of the map to enhance phase-smearing and reduce its peak brightness in order to map faint sources near map center. Only one of the remote HXR sources shows two contour levels, and it is co-located with a TRACE 195 Å feature. Its flux is $< 2\%$ of the main source flux.

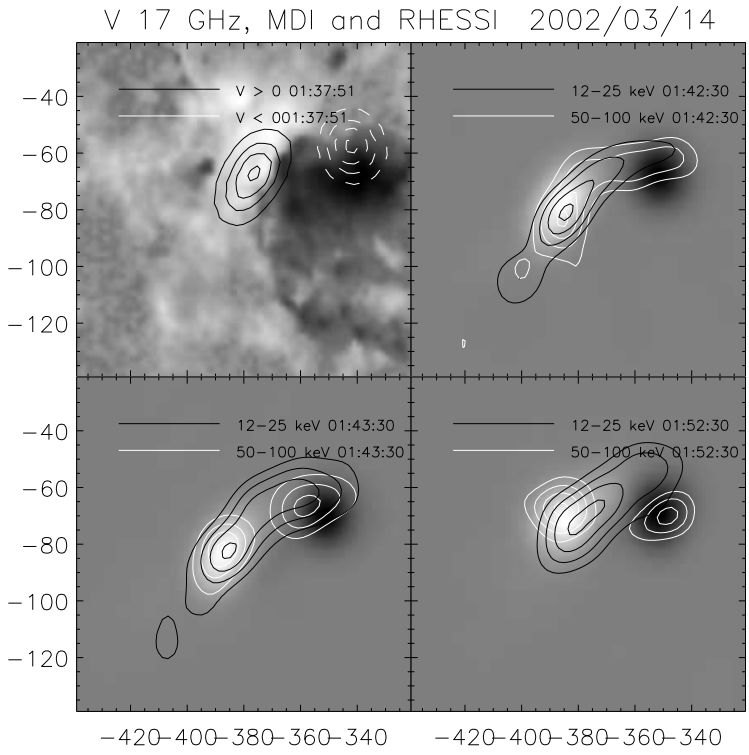

Fig. 10.— Top-left panel: Polarized intensity V (17 GHz) for 01:37:51-01:37:56 UT (contours=30,50,70,90% of local extremum) superposed on an MDI magnetogram at 01:36:30. Other panels: RHESSI 50-100 keV (white) and 12-25 keV (black) contours (40, 55, 70, 85, 99%) of 1-min maps superposed on polarized intensity V(17 GHz) 5-s images (V/I=0.10,-0.046 for white and black, respectively) with integration times 01:42-01:43, 01:43-01:44 and 01:52-01:53. Note the change in orientation of the 50-100 keV footpoints relative to the 12-25 keV loop at 01:52-01:53. The eastern V component appears to move north about 10″ with the HXR footpoint between 01:43:30 and 01:52:30 UT. The RHESSI maps have been made with the same spatial $\sim 6.9''$ resolution as in Fig. 2. The 17-GHz resolution is $\sim 10''$.

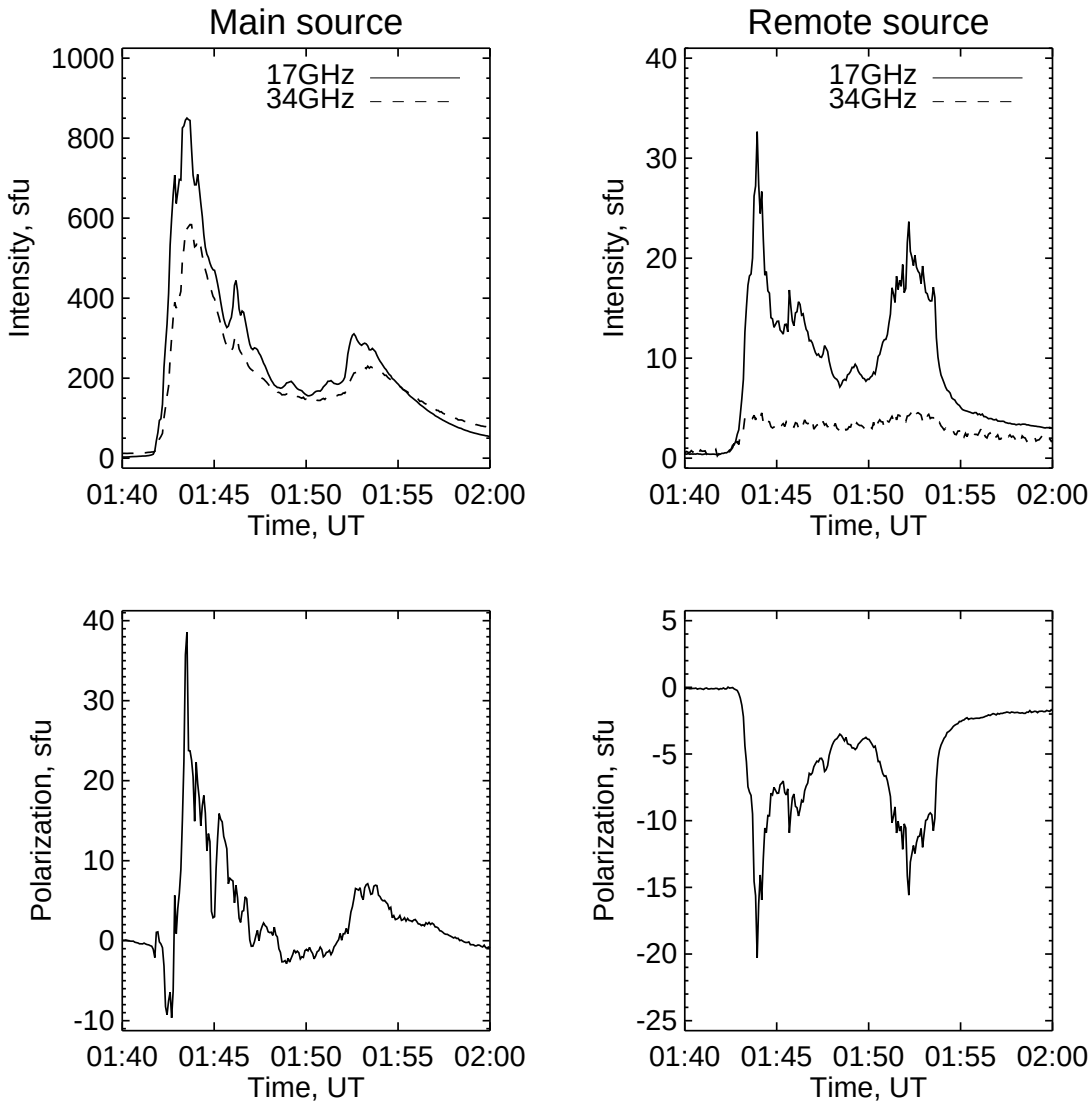

Fig. 11.— Radio I and V time profiles of the main source and remote source. The remote source has a similar time profile to the main source, except that it is oppositely polarized and delayed about 30 s.

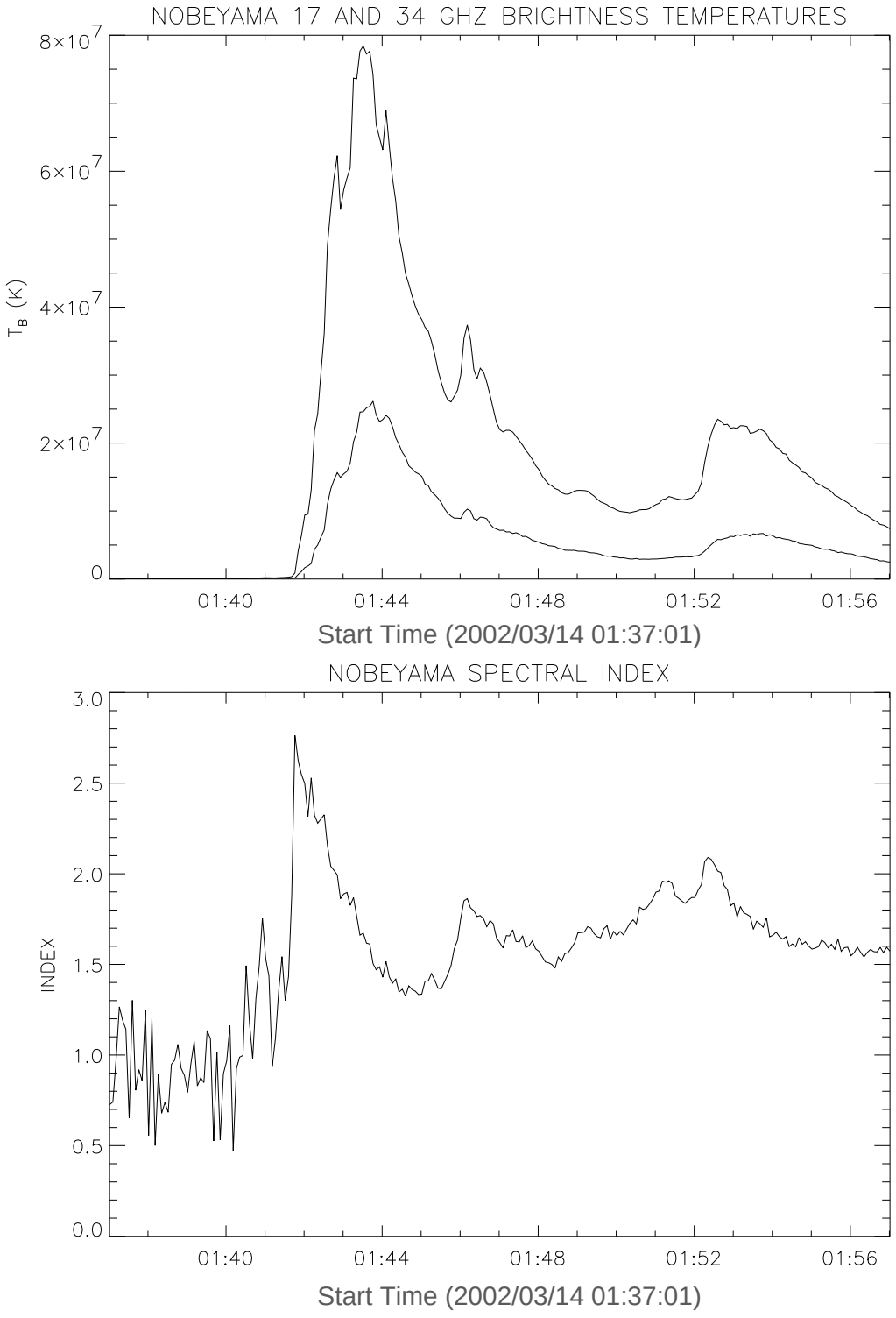

Fig. 12.— Brightness temperature profiles at 17 and 34 GHz, and the derived spectral index.

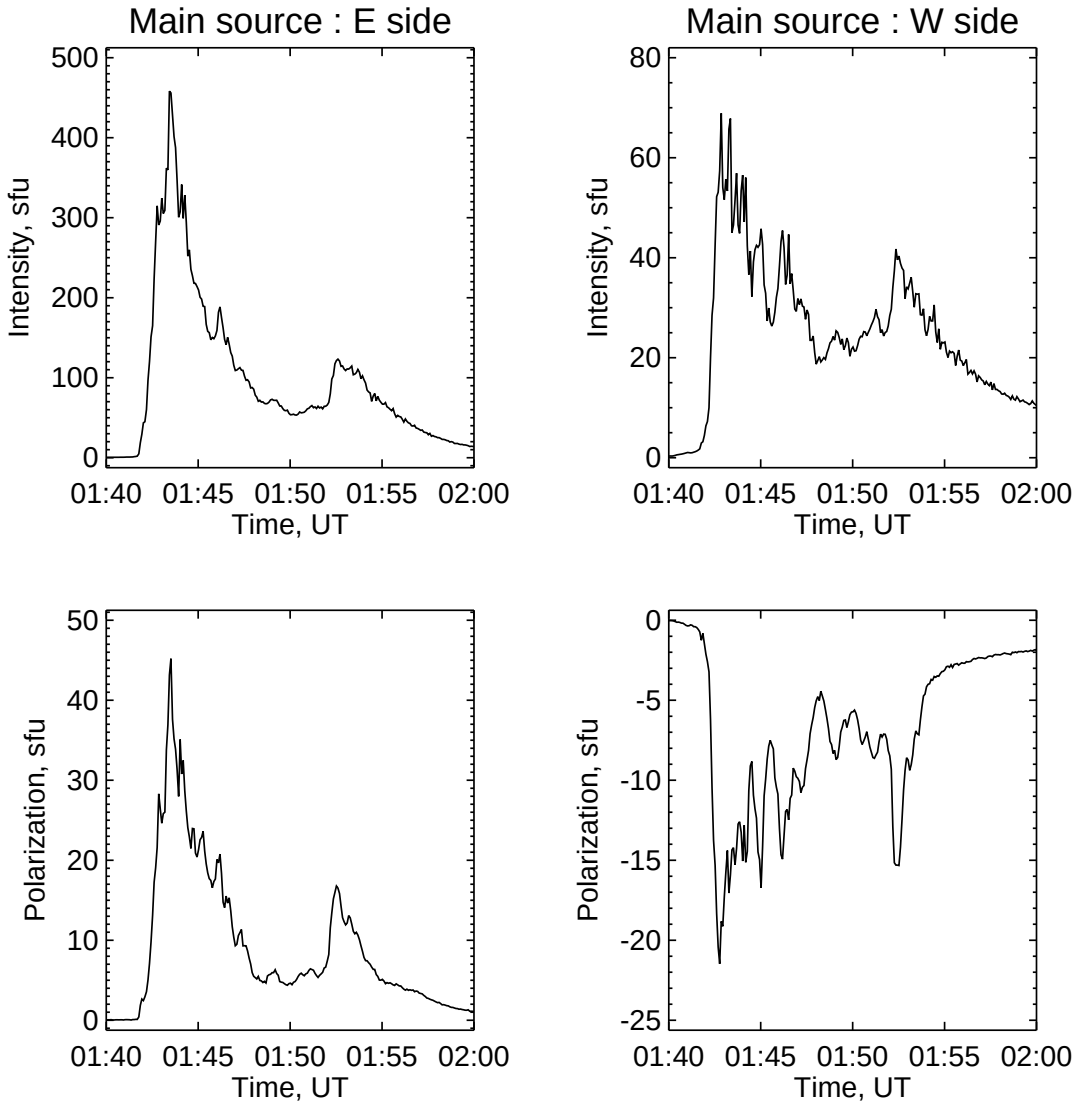

Fig. 13.— 17-GHz time profiles of the east and west sides of the main source.

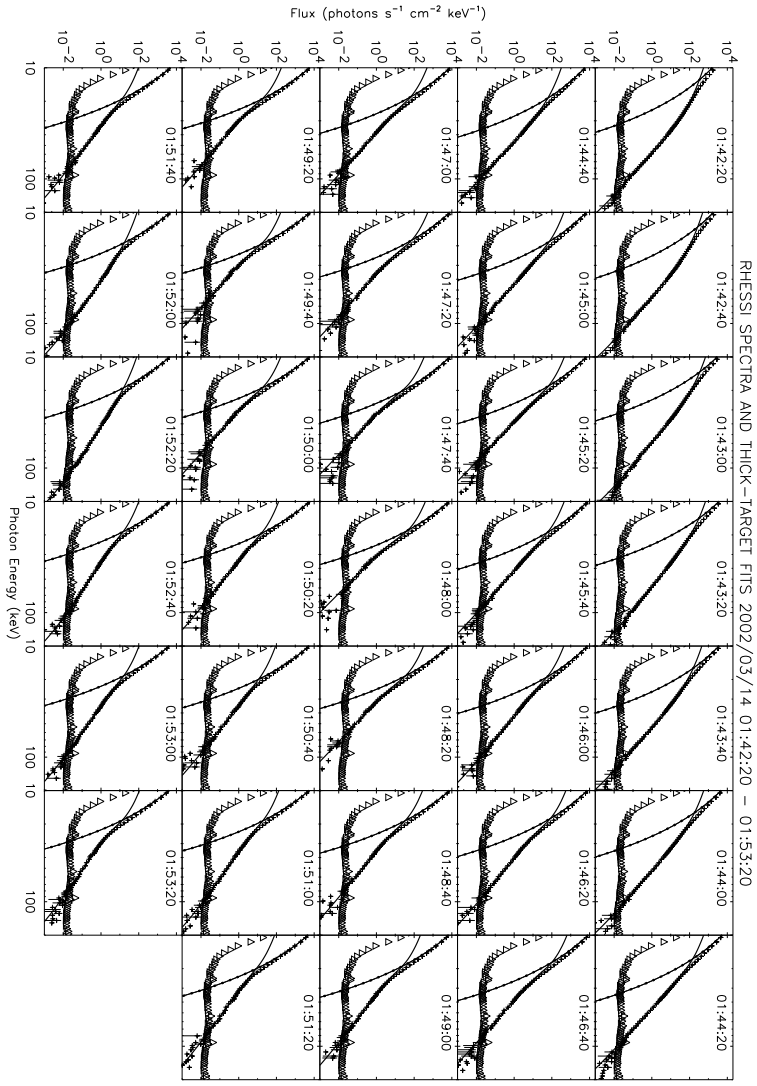

Fig. 14.— Thick-target model fits to the RHESSI spectra, 10-200 keV. Fits to the photon spectra were obtained in 20-s time bins from 01:42:20 to 01:53:20 (start times). The crosses show the photon fluxes and their associated error bars, and the triangles show the background determined for the flare. The parabolic-shaped curves show the thermal component of the model, and the bent, solid curves show the nonthermal component, which is the bremsstrahlung flux from a thick target produced by a broken power-law electron energy spectrum. As discussed in the text, there are 5 variable parameters and 3 constant parameters in the model.

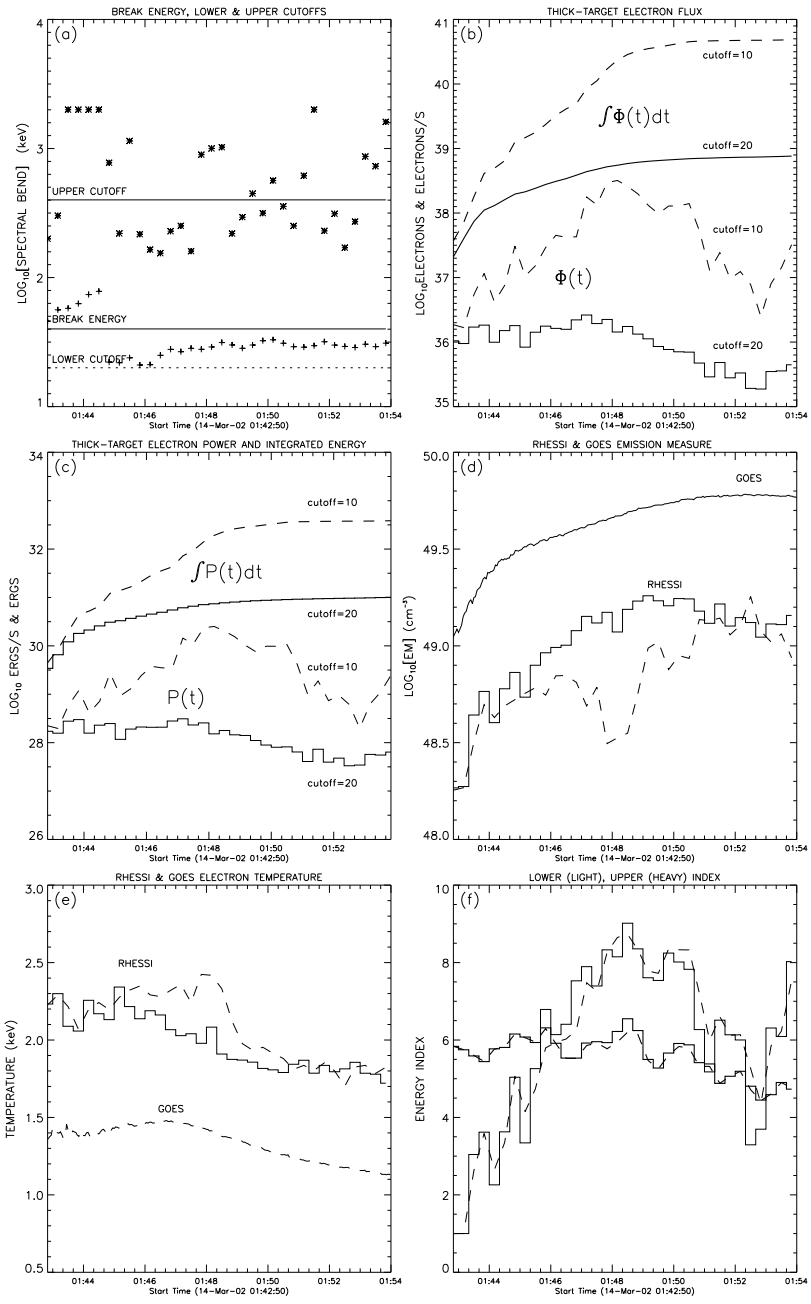

Fig. 15.— Electron distribution parameters from the thick-target model. In all panels the dashed curves are for a model with a 10-keV cutoff, and solid curves are for a 20-keV cutoff. In panel (b), the electron flux (s^{-1}) in the thick target is shown by the lower two curves curves, and the time-integrated flux is shown by the upper curves. Similarly for P(t) and its time integral in (c). The electron spectral index in panel (f) is shown for energies below the break (light curves) and above the break (heavy curves).